Higher harmonic generation of Rayleigh wave at debondings in FRP-retrofitted concrete structures

H. Mohseni and C. T. Ng[1]

School of Civil, Environmental and Mining Engineering, The University of Adelaide, Adelaide, SA 5005, Australia

Abstract

The use of ultrasonic nonlinearity for damage detection and monitoring of structures has attracted growing attention. Interaction of guided waves with contact-type damage, such as debonding, is one of the major sources of ultrasonic nonlinearity. This paper investigates higher harmonic generation of Rayleigh waves in FRP-retrofitted concrete structures due to debonding between FRP and concrete. In this study, propagation and scattering of Rayleigh wave are simulated using a three-dimensional (3D) finite element (FE) method. The numerical simulations of both linear and nonlinear Rayleigh wave are validated with experimentally measured data. There is very good agreement between numerical and experimental results. This paper also investigates the scattering directivity patterns of second and third harmonics of Rayleigh wave. The results provide physical insights into nonlinear Rayleigh wave generated by debonding between FRP and concrete. Overall, the findings of this study can further advance the damage detection methods using the nonlinear Rayleigh wave.

Keywords: Rayleigh wave; FRP-retrofitted concrete; debonding; contact nonlinearity; nonlinear guided wave; higher harmonic

[1] Corresponding author, Email address: alex.ng@adelaide.edu.au

1. Introduction

Structural safety is of paramount importance as evidenced by extensive research work on Structural Health Monitoring (SHM) carried out in the last two decades [1]-[3]. SHM provides a real-time assessment of safety and integrity of engineering structures. Among different SHM techniques, guided wave approach has been recognized as one of the most promising damage detection techniques [4]-[7]. Guided waves offer considerable advantages over conventional bulk wave methods. For example, guided waves can propagate over long distance to achieve large area coverage and allow inspection of inaccessible locations. Guided waves are also sensitive to different types of damages, such as crack [8]-[10], delamination [11]-[13], notch [14], disbonding [15] and corrosion [16]-[18]. Depending on geometry of the waveguide, different types of guided waves can be generated. For example, Rayleigh waves propagate along the surface of a semi-infinite medium and Lamb waves propagate in plate-like structures.

1.1. Linear Rayleigh wave

Applications of Rayleigh wave for damage detection offer significant advantages because the major portion of the wave energy is concentrated along or near the surface, which makes Rayleigh wave ideal for surface or near-surface defect detection [19]-[26]. A number of studies have been carried out to identify surface defects in concrete structures using Rayleigh wave. Hevin *et al*. [21] carried out a numerical study using Rayleigh wave to characterize concrete surface cracks. Edwards *et al*. [22] worked on depth gauging on concrete surface cracks using low frequency wideband Rayleigh wave. Sun *et al*. [23] carried out a study on SHM and defect detection in concrete structures using Rayleigh wave actuated and sensed by piezoceramic transducers. Aggelis *et al*. [24] identified the depth of concrete surface crack and also provided a repair evaluation of concrete using Rayleigh wave. Lee *et al*. [25] presented a method for estimation of concrete crack depth based on Rayleigh wave. Mohseni and Ng [26] proposed to detect and locate debonding in fibre reinforced polymer (FRP) retrofitted concrete structures using the time-of-flight information of linear Rayleigh wave.

Numerical studies were carried out to demonstrate the performance of the proposed debonding detection method. It should be noted that the abovementioned studies only focused on linear Rayleigh wave mostly in concrete structures.

1.2. Nonlinear Rayleigh wave

In the recent years, the concept of ultrasonic nonlinearity has attracted growing attention from researchers because of its potentials of baseline-free damage identification and high sensitivity to early stage of defects [27],[28]. Upon interaction of guided waves with a contact-type defect, such as crack [29]-[31] and delamination [32],[33], the compressive and tensile components of the signal close and open the contact-type defect, respectively. Therefore, the compressive component passes through the defect while the tensile component is reflected. This phenomenon is referred to as contact nonlinearity, which contributes to generation of higher harmonics with frequency at twice, three times or more of the excitation frequency.

For nonlinear Rayleigh wave, Zhang *et al*. [34] carried out a study on higher harmonic generation of Rayleigh wave due to surface scratches in glass. Kawashima *et al*. [35] worked on nonlinear Rayleigh wave due to surface cracks in aluminium using a numerical model and experimental measurements. Yuan *et al*. [36] presented a numerical model of simulating higher harmonics of Rayleigh wave generated by closed cracks. Besides, a number of studies have been performed on material nonlinearity in aluminium [37], titanium [38] and steel [39] using Rayleigh wave.

1.3. Debonding detection for FRP-retrofitted concrete structures

The use of FRP composites to retrofit concrete structures has grown dramatically in the last decade [39],[40]. Advantages of FRP composites are ease of preparation and application, high specific stiffness and specific strength, adjustable mechanical properties, and good resistance to corrosion. However, there is serious concern over long-term performance of the FRPs retrofitted on the

concrete structures [42],[43]. Debonding between FRP and concrete interface is one of the major types of defect in FRP-retrofitted concrete structures, which can be caused by imperfections in raw materials, inappropriate preparation and installation of FRP on the concrete substrate. Also, debonding can be initiated during service life of the retrofitted structure mainly due to environmental factors [44]-[46]. Conventional non-destructive testing techniques, such as visual inspection and tap testing, have been commonly employed to inspect FRP-retrofitted concrete structures [47]. Although these methods are simple and readily available, they are highly subjective and susceptible to misconception, and misunderstanding of operator. Therefore, more accurate damage identification methods need to be developed to inspect FRP-retrofitted concrete structures.

The literature on damage identification in FRP-retrofitted concrete structures using Rayleigh wave has been very limited. As discussed in section 1.1, majority of the existing studies focused on using linear Rayleigh wave to detect damage in concrete structures. For FRP-retrofitted concrete structures, Mohseni and Ng [48] carried out a scattering analysis of linear Rayleigh wave interacting with debonding at FRP/concrete interface. Their study only focused on linear Rayleigh wave. The use of linear Rayleigh wave requires baseline subtraction, which employs reference data to extract the damage information from the measured signals. Varying temperature and loading condition of the structures can limit practical implementation of linear Rayleigh wave [48],[49]. Different to linear Rayleigh, damage detection using nonlinear Rayleigh wave relies on the higher harmonic generation. There is potential that the baseline subtraction is not required to extract the damage information, and hence, it can be a reference-free approach.

The current paper explores applications of nonlinear Rayleigh wave for reference-free damage detection in FRP-retrofitted concrete structures. To the best of the author's knowledge, the use of the nonlinear Rayleigh wave for detecting debonding in FRP-retrofitted concrete structures has not yet been studied thoroughly in the literature. Thus, one of the objectives of this study is to investigate the feasibility and performance of using nonlinear Rayleigh wave for debonding detection in FRP-retrofitted concrete structures.

This paper focuses on higher harmonics generation of Rayleigh wave due to contact

nonlinearity at debonding in FRP-retrofitted concrete structures. A three-dimensional (3D) finite element (FE) model is proposed to predict and investigate the higher harmonic generation phenomenon when the Rayleigh wave interacts with the debonding. In this study, the FE model is first verified with theoretical solutions and experimental measurements for both linear and nonlinear characteristics of Rayleigh wave. The validated 3D FE model is then used in parametric study to investigate the higher harmonic generation characteristics. The findings in this study gain physical insights into the higher harmonics generation of Rayleigh wave at debonding, which can further advance the debonding detection techniques in FRP-retrofitted concrete structures using nonlinear Rayleigh wave.

This paper is organised as follows. The details of the 3D FE model of FRP-retrofitted concrete structures are described in Section 2. The FE simulated results of the linear and nonlinear Rayleigh wave are theoretically and experimentally verified in Section 3. The velocity of the Rayleigh wave is verified using theoretical solutions. In the experimental verification, the 1D laser Doppler vibrometer is used to measure the Rayleigh wave in the FRP-retrofitted concrete structures. Directivity patterns of second and third harmonics of Rayleigh wave are presented in Section 4 based on the experimentally validated 3D FE model. Different sizes of debondings are then investigated in this section. Finally, conclusions of this study are drawn in Section 5.

2. Three-dimensional finite element method

The explicit module of ABAQUS version 6.14 was used to simulate the actuation and propagation of Rayleigh waves in FRP-retrofitted concrete structures. In the 3D FE model, solid and shell elements were used to model concrete and FRP parts, respectively. The dimensions of the 4-ply FRP composite are 300mm×400mm (W×L) and the thickness of each ply is 0.5mm. The stacking sequence of the FRP composite is $[0]_4$. The elastic properties of each lamina are shown in Table 1. The FRP was meshed using 1mm×1mm S4 shell elements. The results of the FE model will be verified by experimental measurements in Section 3. However, if the FE model with the element

size of 1 mm has the same dimension as the test specimen, the required computational cost will be extremely high. Therefore, in the FE model, the dimensions of the concrete block are 300mm×400mm×150mm (W×L×H). The Young's modulus and density of concrete are 26.8GPa and 2350kg/m^3, respectively. The concrete was meshed using 1mm×1mm×1mm C3D8 solid elements. The FRP and concrete are connected by tie constraint. The debonding was created by removing the tie constraint over debonding area. A surface-to-surface frictionless hard contact was used to simulate clapping effect at the debonding. Figure 1 shows the schematic diagram of the numerical model.

[**Table 1**. Elastic properties of FRP lamina]

[**Figure 1**. Schematic diagram of the FE model]

The Rayleigh wave was actuated by applying radial displacements on nodes located on the circumference of the upper surface of a 2mm thick and 10mm diameter circular piezoceramic transducer. The Young's modulus, density and Poisson's ratio of the piezoceramic transducer are 58.8GPa, 7700kg/m^3 and 0.39, respectively. The piezoceramic transducer was meshed using 1mm×1mm×1mm C3D8 elements in the FE model. The excitation signal is a 15-cycle tone burst modulated by a Hanning window [51]. The central excitation frequency for both numerical simulations and experimental measurements is 95kHz. Since the out-of-plane motion is dominant in the Rayleigh wave propagation, the wave signals were measured based on out-of-plane nodal displacements at measurement points on FRP composite. This element size of the FE model ensures the accuracy of the numerical simulations for the linear and second harmonic Rayleigh wave since it has enough number of elements per wavelength for the linear and second harmonic Rayleigh wave. For the third harmonic, there are only around seven elements per wavelength. The accuracy of the FE simulated results will then be validated theoretically and experimentally in Section 3.

Figure 2 shows the typical contour snapshots of the FE simulated displacement at the

FRP-retrofitted concrete. Figure 2a shows the piezoceramic transducer generated Rayleigh wave and the wave interaction with the debonding. Figures 2b, 2c and 2d show the simulated displacement at time $t = 1.03\times10^{-4}$sec, $t = 1.22\times10^{-4}$sec, and $t = 1.41\times10^{-4}$sec, respectively. The figures show that when the Rayleigh wave interacts with the debonding, the clapping effect happens between the FRP and concrete.

[**Figure 2**. Contour snapshots of FE simulated displacement at time a) $t = 1.03\times10^{-4}$sec, b) the zoom-in of the cross-section at the debonding; c) $t = 1.22\times10^{-4}$sec; and d) $t = 1.41\times10^{-4}$sec]

3. Theoretical and experimental validation of 3D FE model

3.1. Theoretical verification

DISPERSE computer program [52] was used to theoretically verify the numerical results simulated by the 3D FE model described in Section 2. DISPERSE employs global matrix method to calculate velocity of Rayleigh wave in multi-layer waveguides. In this method, guided wave in each layer is expressed as the combination of partial waves. Displacements and stresses at any location of each layer are expressed as a function of partial waves using a field matrix. The field matrix of each layer can be obtained from material properties of the layer. The whole system is modelled by assembling the field matrices of all layers. This solution is based on consistency of displacements and stresses at interfaces of layers. Therefore, propagation of Rayleigh wave in the FRP-retrofitted concrete model without debonding can be theoretically validated. In this study, the phase velocity of Rayleigh wave in FRP-retrofitted concrete model is obtained by DISPERSE and compared with the FE results as shown in Figure 3. There is good agreement between numerical and theoretical results.

[**Figure 3**. Numerical and theoretical results of the Rayleigh wave phase velocity dispersion curve]

3.2. Experimental setup

Experimental measurements were carried out on the concrete block with dimensions of 300mm×600mm×300mm (W×L×H). The Young's modulus and density of the concrete are 26.8GPa and 2350kg/m^3, respectively. The maximum size of the concrete aggregate is 10mm. The FRP composite consists of four unidirectional carbon fibre layers with dimensions of 300mm×600mm and the stacking sequence is $[0]_4$. The BASF MasterBrace 4500 epoxy resin was applied to saturate carbon fabric layers. The hand lay-up method was used to bond saturated fibre layers on the concrete block. The debonding between FRP and concrete was created by inserting 40mm×300mm Mylar sheet on the concrete before application of the first fibre layer. The debonding was located between x = 280mm and x = 320mm based on the Cartesian coordinate shown in Figure 1, and is across whole width of the concrete block.

A 2mm thick and 10mm diameter circular piezoceramic transducer was used to actuate Rayleigh wave. The piezoceramic transducer is made of Ferroperm Pz27, which has the same mechanical properties used in the FE simulations described in Section 2. The actuator was bonded to the FRP surface at x = 200mm and z = 150mm. The excitation signal is a 15-cycle tone burst modulated by a Hanning window wave, which is the same as the excitation signal used in the FE simulations. The excitation signal was generated by a Tektronix AFG 3021B arbitrary function generator. The amplitude of the generated signal was 10V (peak-to-peak), which was then amplified five times by a KROHN-HITE 7500 amplifier. The Rayleigh wave signals were measured using Polytec PSV-400 1D laser Doppler vibrometer system. The laser head controlled by vibrometer controller captured the out-of-plane displacements. The data was recorded by a data acquisition unit and fed into the PC. The sampling frequency of the measurement was set to 10.24MHz. A bandpass filter of frequency band 10kHz-600kHz was applied to the measured signals. Considering the excitation frequency of 95kHz, the frequency band of the bandpass is wide enough to capture the higher harmonics. In order to increase the signal-to-noise ratio, an averaging of 5000 times was applied to the measured signals. A schematic diagram of the experimental setup is shown in Figure 4. Figure 5 displays a full setup of measuring Rayleigh wave on FRP-retrofitted concrete specimen

using laser Doppler vibrometer. Figure 6 shows the dimension of the specimen and location of the debonding, actuator and measurement point. The corresponding size of the FE model is also indicated in Figure 6.

[**Figure 4**. Schematic diagram of experimental setup]

[**Figure 5**. Experimental setup and laser Doppler vibrometer]

[**Figure 6**. FE model and experimental specimen used in the experimental validation]

3.3. Higher harmonics generation due to contact nonlinearity at debonding

For the numerical model in this section, the debonding is 40mm×300mm with left and right end at x = 180mm and x = 220mm, respectively, and across the whole width of the concrete block. Based on the cylindrical coordinate shown in Figure 1, the actuator is located at r = 100mm and θ = 180° away from the debonding centre. For both FE simulation and experiment, the measurement point is at r = 50mm and θ = 0° away from the debonding centre. Figure 7 compares the FE simulated and experimentally measured Rayleigh wave signals in the time-domain. There is good agreement between numerical and experimental results.

[**Figure 7**. Time-domain Rayleigh wave signal obtained from FE simulation and experimental measurement]

To compare the generated higher harmonic due to the contact nonlinearity at the debonding, , the measured time-domain numerical and experimental signals are transformed to frequency-domain using fast Fourier transform (FFT) [52]. The time-domain signals contain incident wave and wave reflections from boundaries. Thus, the scattered wave from the debondings,

caused by the incident wave and wave reflected from boundaries, can contribute to the generation of higher harmonics in the frequency-domain. As explained above, the FE model has the same width but smaller length than experimental specimen. Therefore, the wave reflections from the boundaries in FE simulation are different to the experiment. On the other hand, the location of the actuator and the measurement point with respect to the debonding is similar in the FE simulation and experiment. Considering the arrangement for actuating and sensing the signals, the FE model is large enough to avoid the nonlinear Rayleigh wave induced by the interaction of the incident wave and reflected signals from the boundaries with the debonding, being mixed at the measurement point. With considering a specific time duration, the signal obtained at the measurement point can contain only incident wave and the scattered incident wave at the debonding. Thus, the higher harmonics can be compared between the numerically calculated and experimentally measured data.

In addition to the contact nonlinearity [54], the higher harmonics in the measured Rayleigh wave signals can be caused by experimental instrument and also nonlinearity of materials [55],[56]. In the literature, it has been confirmed that the instrument nonlinearity has a negligible effect on higher harmonics of the experimentally measured Rayleigh waves [57],[58]. It is assumed that the experimentally measured higher harmonics in this study are mainly due to contact nonlinearity at the debonding between the FRP and concrete interface. In this study, higher harmonics of the signal obtained from the intact specimen (without debonding) were also examined, and they are very small compared to higher harmonics induced by the debonding.

To investigate the higher harmonics, the measured signals were transformed from time-domain to the frequency-domain using FFT. It should be noted that the FFT was only applied to the signal from t = 0sec until t = 2.3×10^{-4}sec. Within this time duration, the signal mainly contains incident wave and scattered wave from the debonding caused by the incident wave. Therefore, this ensures the higher harmonics in the signals are only due to the incident wave interaction with the debonding.. Figure 8 shows the normalized FFT amplitude of numerically calculated and experimentally measured signals. Considering the excitation frequency of 95kHz, the second harmonic and third harmonic frequency are 190kHz and 285kHz, respectively. Figure 8

shows a comparison between the numerically simulated and experimentally measured data. In addition to the FE model using fully integrated elements (S4 shell elements and C3D8 solid elements), the results obtained from a FE model using reduced-integration elements (S4R shell elements and C3D8R solid elements), are presented in Figure 8 to demonstrate the accuracy between the fully integrated elements and reduced-integration elements in predicting higher harmonic generation. It is shown that the FE results using the reduced-integration elements have larger discrepancies between the numerically calculated and experimentally measured amplitude of the second harmonic. For the FE results using fully integrated elements, there is good agreement between the numerically calculated and experimentally measured second and third harmonic magnitudes. There exists a small discrepancy and this may be caused by the effect of the Mylar film, which was not modelled in the FE simulation.

[**Figure 8**. Fourier transformed FE simulated and experimentally measured Rayleigh wave signals]

4. Directivity patterns of higher harmonic generation at debonding in FRP-retrofitted concrete structures

The experimentally and theoretically validated FE model is used in the parametric studies. Based on the cylindrical coordinate system shown in Figure 1, the Rayleigh wave is generated at r = 100mm and $\theta = 0°$. Considering the Cartesian coordinate in Figure 1, the actuator is located at x = 100mm and z = 150mm. Square debondings with sizes of 8mm, 14mm, 22mm, 30mm, 38mm and 44mm are considered in the case studies. In all debonding cases, the centre of the debonding is located at r = 0mm and the debonding edges are parallel to the x- and y-axis. To study the effect of the debonding size on the directivity pattern of the generated higher harmonics, the results are presented in terms of debonding size to wavelength ratio (R_{DW}). The out-of-plane displacements are monitored at 36 points at r = 50mm and $0° \leq \theta \leq 360°$ with intervals of 10°.

To investigate the measured signals in time-frequency domain, energy density spectra of the signals are obtained using short-time Fourier transform (STFT). Figures 9 and 10 show the energy density spectrum of the signal for the case with square debonding size of 38mm at $\theta = 30°$, and 22mm at $\theta = 330°$, respectively. Second and third harmonics of the Rayleigh wave are visible in the energy density spectra.

[**Figure 9**. Energy density spectrum in time-frequency domain for debonding size of 38×38 mm and θ =30°]

[**Figure 10**. Energy density spectrum in time-frequency domain for debonding size of 22×22 mm and θ =330°]

For each debonding case, the amplitudes of the fundamental harmonic (f_0), the second harmonic ($2f_0$) and the third harmonic ($3f_0$) are obtained from the energy density spectrum at the respective frequencies. The ratio of the second harmonic amplitude to the fundamental harmonic amplitude (A_2/A_1), and ratio of the third harmonic amplitude to the fundamental harmonic amplitude (A_3/A_1) are considered. These ratios for each debonding case are presented against θ in the form of directivity pattern. Figure 11 displays the directivity patterns of A_2/A_1 ratio for different sizes of square debonding. The directivity patterns show that the A_2/A_1 ratio is almost evenly distributed in forward and backward directions for smaller size of debonding, such as Figure 10a. When the debonding size increases, the magnitudes of the A_2/A_1 ratios increase in the forward direction. Figure 12 displays the directivity patterns of A_3/A_1 ratio for the same sizes of the aforementioned debonding. The figures show that the magnitudes of the A_3/A_1 ratios are usually higher in the forward directions.

[**Figure 11**. Directivity pattern for second harmonic amplitude to fundamental harmonic amplitude ratio (A_2/A_1) for debonding size a) 8mm×8mm, b) 14mm×14mm, c) 22mm×22mm, d) 30mm×30mm, d) 38mm×38mm, and f) 44mm×44mm]

[**Figure 12**. Directivity pattern for third harmonic amplitude to fundamental harmonic amplitude ratio (A_3/A_1) for debonding size a) 8mm×8mm, b) 14mm×14mm, c) 22mm×22mm, d) 30mm×30mm, d) 38mm×38mm, and f) 44mm×44mm]

Figures 13 and 14 show the higher harmonic amplitudes of Rayleigh wave with respect to R_{DW} at different directions. Figures 13 and 14 present the results in Figures 11 and 12 in a different way, which is used to show the relationship between the higher harmonic magnitude and debonding size. Figure 13a shows the A_2/A_1 ratio in the forward scattering direction as a function of R_{DW} At θ = 0°, the A_2/A_1 ratio starts with a rapid rise and a then a sharp drop until R_{DW} =1. After that, it increases constantly to a peak of 0.0864 at R_{DW} = 2. At θ = 30° and θ = 330°, the A_2/A_1 ratio first increases sharply to a peak of 0.0683 and then decreases steeply to 0.0343 at R_{DW} = 1. It then shows some fluctuations with a decreasing trend. The A_2/A_1 ratio at θ = 60° and θ = 300° drops slowly until R_{DW} = 1, and then exhibits moderate fluctuations.

The A_2/A_1 ratio in the backward scattering direction as a function of R_{DW} is shown in Figure 13b. The A_2/A_1 ratios at θ = 120°, θ = 240°, θ = 150°, θ = 210° and θ = 180° show slight fluctuations. As shown in Figure 12b, the A_2/A_1 ratio at θ = 150°, θ = 210° and θ = 180° is slightly bigger than that at θ = 120° and θ = 240°

Figure 14a shows the A_3/A_1 ratio in the forward direction as a function of R_{DW}. At θ = 0°, the A_3/A_1 ratio begins with a sudden rise, next a sharp drop, and then a steep increase to a peak of 0.0420 at R_{DW} = 1.36. Then, it decreases slowly to 0.0375 at R_{DW} = 2. At θ = 30° and θ = 330°, the A_3/A_1 ratio first increases rapidly to 0.0335 and then falls gradually to 0.0229 at R_{DW} = 1.36. Then, it increases steadily to a peak of 0.0416 at R_{DW} = 1.73. The A_3/A_1 ratio at θ = 60° and θ = 300° is

notably smaller than amplitude ratio at $\theta = 0°$, $\theta = 30°$ and $\theta = 330°$ while exhibiting moderate fluctuations.

Figure 14b displays the A_3/A_1 ratio in the backward scattering direction as a function of R_{DW}. At $\theta = 150°$, $\theta = 210°$ and $\theta = 180°$, it is obvious that the A_3/A_1 ratio in the backward scattering direction is markedly smaller than that of A_2/A_1 ratio and it fluctuates around 0.006-0.009. However, at $\theta = 120°$ and $\theta = 240°$, the amplitude starts with small values and slight fluctuations until $R_{DW} = 1.36$. After that, it increases steadily to a peak of 0.0024, and then falls steeply to 0.0062 at $R_{DW} = 2$.

The overall trends of the second harmonic and third harmonic of the Rayleigh wave in the forward and backward scattering direction are discussed for the cases of square debondings. For smaller values of R_{DW}, the A_2/A_1 ratio has larger values at $\theta = 30°$ and $\theta = 330°$ than $\theta = 0°$. However, for $R_{DW} > 1.36$, the largest values of A_2/A_1 ratio are at $\theta = 0°$. The maximum values of A_3/A_1 ratio in the forward scattering direction occur at $\theta = 0°$, and then at $\theta = 30°$ and $\theta = 330°$. In general, the second and third harmonics in backward scattering direction have smaller amplitudes than that in the forward scattering direction. Besides, it is obvious that the third harmonic in the backward scattering direction are smaller than that of second harmonic for cases of square debondings. In general, both second and third harmonic in backward scattering direction are not very sensitive to change of the debonding size. Based on the results, the second and third harmonic in forward scattering direction are more suitable to be used in the debonding identification. In general, the second harmonic is more sensitive than third harmonic to the debonding sizes.

[**Figure 13**. Second harmonic amplitude to fundamental harmonic amplitude ratio (A_2/A_1) in the a) forward and b) backward scattering direction as a function of debonding size to wavelength ratio]

[**Figure 14**. Third harmonic amplitude to fundamental harmonic amplitude ratio (A_3/A_1) in the a) forward and b) backward scattering direction as a function of debonding size to wavelength ratio]

5. Conclusions

This study has investigated the higher harmonic generation of Rayleigh wave at the debondings in FRP-retrofitted concrete structures using experimentally and theoretically verified 3D FE model. The numerical results of Rayleigh wave propagation and scattering have been presented in time, frequency and time-frequency domains. Both second and third harmonics of Rayleigh wave induced by the debonding at FRP and concrete interface have been studied in detail. Very good agreement has been observed between numerically calculated and experimentally measured results. It has been shown that the 3D FE model is capable of simulating Rayleigh wave propagation, scattering, and higher harmonic generation at the debondings.

The experimentally validated 3D FE model has been used in the parametric case studies. Square debondings with different sizes have been investigated. Second and third harmonics in the forward and backward scattering direction have been studied. The second and third harmonic amplitudes have been presented in terms of debonding size to wavelength ratio. For square debondings, the amplitude of the second harmonic is generally larger than that of the third harmonic. Also, the second and third harmonic amplitudes in the forward scattering direction are larger than those in the backward scattering direction. That means that for the second and third harmonics, the energy is mainly concentrated in forward scattering direction.

This study has gained physical insights into the generation of second and third harmonics of Rayleigh wave at debonding in FRP-retrofitted concrete. The study has shown that the results of parametric study could provide a quantitative assessment of the sensitivity of the second and third harmonics of Rayleigh wave in detecting different sizes of debondings. The relationship between the second and third harmonic, and different sizes of debondings can provide valuable information in planning and designing the damage detection techniques using second and third harmonics, for example, the suitable range of excitation frequency in detecting the required sizes of debondings.

The results of the parametric study suggest that the second and third harmonic in forward scattering direction are more sensitive than those in backward scattering direction. It is recommended to use pitch-catch approach, which can fully capture the forward scattered second

and third harmonic Rayleigh wave, in the debonding detection. The results of the parametric study also suggest that the second harmonic is more sensitive than third harmonic in detecting and monitoring the debonding in FRP-retrofitted concrete. Overall, the findings of this study can further advance the developments of nonlinear Rayleigh wave-based debonding detection techniques.

6. Acknowledgment

This work was supported by the Australian Research Council (ARC) under Grant Numbers DP160102233. The supports are greatly appreciated.

7. References

[1] Wandowski T, Malinowski P, Ostachowicz WM. Damage detection with concentrated configurations of piezoelectric transdcuers. Smart Mater Struct 2011;20:025002.

[2] Worden K, Farrar CR, Manson G, Park G. The fundamental axioms of structural health monitoring. Proc Royal Soc A 2007;463:1639-1664.

[3] Lee BC, Staszewski W. Modelling of Lamb waves for damage detection in metallic structures: Part I wave propagation. Smart Mater Struct 2003;12(5):804-814.

[4] Rose JL. A baseline and vision of ultrasonic guided wave inspection potential. J Pressure Vessel Tech 2002;124:273-282.

[5] Giurgiutiu V, Bao J. Embedded-ultrasonics structural radar for in situ structural health monitoring of thin-wall structures. Struct Health Monit 2004;3:121-140.

[6] Clarke T, Cawley P. Enhancing the defect localization capability of a guided wave SHM system applied to a complex structure. Struct Health Monit 2011;10(3):247-259.

[7] He S, Ng CT. A probabilistic approach for quantitative identification of multiple delaminations in laminated composite beam using guided wave. Eng Struct 2017;127:602-614.

[8] Sohn H, Kim SB. Development of dual PZT transducers for reference-free crack detection in thin plate structures. IEEE Trans Ultrason Ferroelectr Freq Control 2009;57(1):229-240.

[9] Kudela P, Radzienski M, Ostachowicz W. Identification of cracks in thin-walled structures by means of wavenumber filtering. Mech Syst Sig Process 2015;50-51:456-466.

[10] He S, Ng CT. Guided wave-based identification of multiple cracks in beams using a Bayesian approach. Mech Syst Sig Process 2017;84:324-345.

[11] Kessler SS, Spearing SM, Soutis C. Damage detection in composite materials using Lamb wave methods. Smart Mater Struct 2002;11:269-278.

[12] Ng CT. On accuracy of analytical modelling of Lamb wave scattering at delaminations in multilayered isotropic plates. Inter J Struct Stab Dyn 2015;5(8):1540010.

[13] Sohn H, Park G, Wait JR, Limback NP, Farrar C. Wavelet-based active sensing for delamination detection in composite structures. Smart Mater Struct 2003;13(1):153-160.

[14] Soleimanpour R, Ng CT. Scattering of the fundamental anti-symmetric Lamb wave at through-thickness notches in isotropic plates. J Civil Struct Health Monit 2016;6:447-459.

[15] Samaratunga D, Jha R, Gopalakrishnan S. wavelet spectral finite element for modelling guided wave propagation and damage detection in stiffened composite panels. Struct Health Monitor 2016;15(3):317-334.

[16] Miller TH, Kundu T, Huang J, Grill JY. A new guided wave-based technique for corrosion monitoring in reinforced concrete. Struct Health Monit 2012;12(1):35-47.

[17] Ng CT. A two-stage approach for quantitative damage imaging in metallic plates using Lamb wave. Earthquakes Struct 2015;8(4):821-841.

[18] Aryan P, Kotousov A, Ng CT, Cazzolato BS. A baseline-free and non-contact method for detection and imaging of structural damage using 3D laser vibrometry. Struct Control Health Monit 2017;24:e1894.

[19] Zerwer A, Polak MA, Santamarina JC. Rayleigh wave propagation for the detection of near surface discontinuities: finite element modelling. J Nondestructive Eva 2003;22(2):39-52.

[20] In CW, Kim JY, Kurtis KE, Jacobs LJ. Characterization of ultrasonic Rayleigh surface waves in asphaltic concrete. NDT & E Inter 2009;42(7):610-617.

[21] Hevin G, Abraham O, Pedersen HA, Campillo M. Characterisation of surface cracks with

Rayleigh waves: a numerical model. NDT&E Inter 1998;31:289-297.

[22] Edwards RS, Dixon S, Jian X. Depth gauging of defects using low frequency wideband Rayleigh waves. Ultrasonics. 2006;44:93-98.

[23] Sun M, Staszewski WJ, Swamy RN, Li Z. Application of low-profile piezoceramic transducers for health monitoring of concrete structures. NDT&E Inter 2008;41:589-595.

[24] Aggelis DG, Shiotani T, Polyzos D. Characterization of surface crack depth and repair evaluation using Rayleigh waves. Cement & Concrete Compos 2009;31:77-83.

[25] Lee FW, Lim KS, Chai HK. Determination and extraction of Rayleigh-waves for concrete cracks characterization based on matched filtering of center of energy. J Sound Vib 2016;363:303-315.

[26] Mohseni H, Ng CT. Rayleigh wave for detecting debonding in FRP-retrofitted concrete structures using piezoelectric transducers. Computer Concrete 2017;20(5):583-593.

[27] Parson Z, Staszewski WJ. Nonlinear acoustics with low-profile piezoceramic excitation for crack detection in metallic structurs. Smart Mater Struct 2006;15(4):1110-1118.

[28] Soleimanpour R, Ng CT. Locating delamination in laminated composite beams using nonlinear guided waves. Eng Struct 2017;131(15):207-219.

[29] Shen Y, Cesnik CE. Modelling of nonlinear interactions between guided waves and figure cracks using local interaction simulation approach. Ultrasonics 2017;74:106-123.

[30] He S, Ng CT. Modelling and analysis of nonlinear guided waves interaction at a breathing crack using time-domain spectral finite element method. Smart Mater Struct 2017;26:085002.

[31] Yang Y, Ng CT, Kotousov A. Influence of crack opening and incident wave angle on second harmon ic generation of Lamb wave. Smart Mater Struct 2018;27:055013.

[32] Yelve NP, Mitra M, Mujumdar PM. Detection of delamination in composite laminates using Lamb wave based nonlinear method. Compos Struct 2017;159:257-266.

[33] Soleimanpour R, Ng CT, Wang CH. Higher harmonic generation of guided waves at delaminations in laminated composite beams. Struct Health Monit 2017;16(4):400-417.

[34] Zhang J, Xuan F-Z, Yang F. Effect of surface scratches on the characteristics of nonlinear

Rayleigh surface waves in glass. J Non-Crystalline Solids 2013;378:101-105.

[35] Kawashima K, Omote R, Ito T, Fujita H, Shima T. Nonlinear acoustic response through minute surface cracks: FEM simulation and experimentation. Ultrasonics 2002;40:611-615.

[36] Yuan M, Zhang J, Song SJ, Kim HJ. Numerical simulation of Rayleigh wave interaction with surface closed cracks under external pressure. Wave Motion. 2015;57:143-153.

[37] Shui G, Kim J-Y, Qu J, Wang Y-S, Jacobs LJ. A new technique for measuring the acoustic nonlinearity of materials using Rayleigh waves. NDT&E International. 2008;41:326-329.

[38] Guo S, Zhang L, Mirshekarloo MS, Chen S, Chen YF, Wong ZZ, et al. Method and analysis for determining yielding of titanium alloy with nonlinear Rayleigh surface waves. Materials Science and Engineering: A. 2016;669:41-47.

[39] Doerr C, Kim J-Y, Singh P, Wall JJ, Jacobs LJ. Evaluation of sensitization in stainless steel 304 and 304L using nonlinear Rayleigh waves. NDT & E International. 2017;88:17-23.

[40] Smith ST, Teng JG. FRP-strengthened RC beams I: review of debonding strength models. Eng Struct 24(4):385-395.

[41] Rahimi H, Hutchinson A. concrete beams strengthened with externally bonded FRP plates. J Compos Const 2001;5(1):44-56.

[42] Hollaway LC. A review of the present and future utilisation of FRP composites in the civil infrastructure with reference to their important in-service properties. Construction Build Mater. 2010;24:2419–2445.

[43] Brown JR, Hamilton HR. Quantitative infrared thermography inspection for FRP applied to concrete using single pixel analysis. Construction Build Mater 2013;38:1292-1302.

[44] Akuthota B, Hughes D, Zoughi R, Myers J, Nanni A. Near-field microwave detection of disbond in carbon fiber reinforced polymer composites used for strengthening cement-based structures and disbond repair verification. J Mater Civil Eng 2004;16:540-546.

[45] Nassr AA, Dakhakhni WWE. Damage detection of FRP-strengthened concrete structures using capacitance measurements. J Compos Construction. 2009;13:486-497.

[46] Mahmoud AM, Ammara HH, Mukdadi OM, Ray I, Imani FS, Chen A, et al. Non-destructive

ultrasonic evaluation of CFRP–concrete specimens subjected to accelerated aging condition. NDT & E Inter 2010;43:635-641.

[47] Telang NM, Dumlao C, Mehrabi AB, Ciolko AT, Gutierrez J. Field inspection of in-service FRP bridge decks- NCHRP report 564: National Cooperative Highway Research Program 2006.

[48] Mohseni H and Ng CT. Rayleigh wave propagation and scattering characteristics at debondings in FRP-retrofitted concrete structures. Struct Health Monit 2018; (10.1177/1475921718754371)

[49] Mohabuth M, Kotousov A, Ng CT. Effect of uniaxial stress on the propagation of higher-order Lamb wave mdoes. Inter. J. Non-linear Mech 2016;86:104-111.

[50] Mohabuth M, Kotousov A, Ng CT, Rose LRF. Implication of changing loading conditions on structural health monitoring utilising guided waves. Smart Mater. Struct 2018;27:025003.

[51] Aryan P, Kotousov A, Ng CT, Cazzolato B. A model-based method for damage detection with guided waves. Struct Control Health Monit 2017;24:e1884.

[52] Pavlakovic B, Lowe M. DISPERSE version 2.0.16 User's Manual. Imperial College NDT Laboratory; 2003.

[53] Coverley PT, Staszewski WJ. Impact damage location in composite structures using optimized sensor triangulation procedure. Smart Mater Struct 2003;12:795-803.

[54] Yang Y, Ng CT, Kotousov A, Sohn H, Lim HJ. Second harmonic generation at fatigue cracks by low-frequency Lamb waves: Experimental and numerical studies. Mech Syst Signal Process 2018;99:760-773.

[55] Van Den Abeele KEA, Carmeliet J, Ten Cate JA, Johnson PA. Nonlinear elastic wave spectroscopy (NEWS) techniques to discern material damage, part II: single-mode nonlinear resonance acoustic spectroscopy. Res NDE 2000;12:31-42.

[56] Scalerandi M, Agostini V, Delsanto PP. Local interaction simulation approach to modelling nonclassical, nonlinear elastic behaviour in solids. J Acoust Soc Am 2003;113:3049.

[57] Kim G, In C-W, Kim J-Y, Kurtis KE, Jacobs LJ. Air-coupled detection of nonlinear Rayleigh surface waves in concrete-Application to microcracking detection. NDT & E Inter 2014;67:64-70.

[58] Torello D, Thiele S, Matlack KH, Kim J-Y, Qu J, Jacobs LJ. Diffraction, attenuation, and source corrections for nonlinear Rayleigh wave ultrasonic measurements. Ultrasonics 2015;56:417-426.

Table

[**Table 2**. Elastic properties of FRP lamina]

E	E_{22}	G_1	G	ν_{12}	ν	ρ
7	5.9	2.1	2	0.3	0	1

Figures

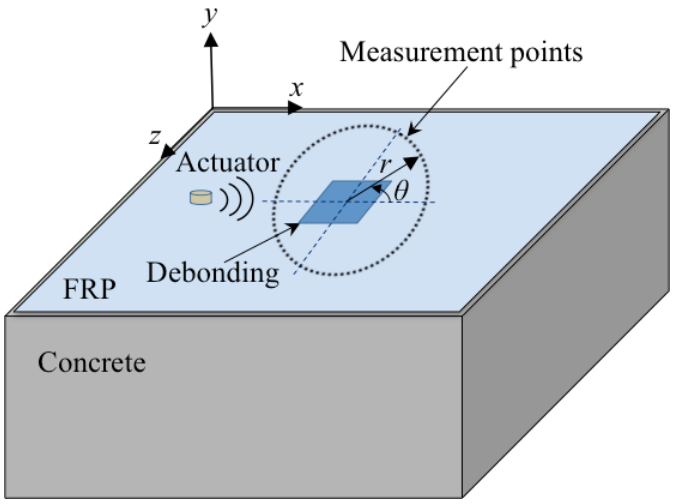

[**Figure 15**. Schematic diagram of the FE model]

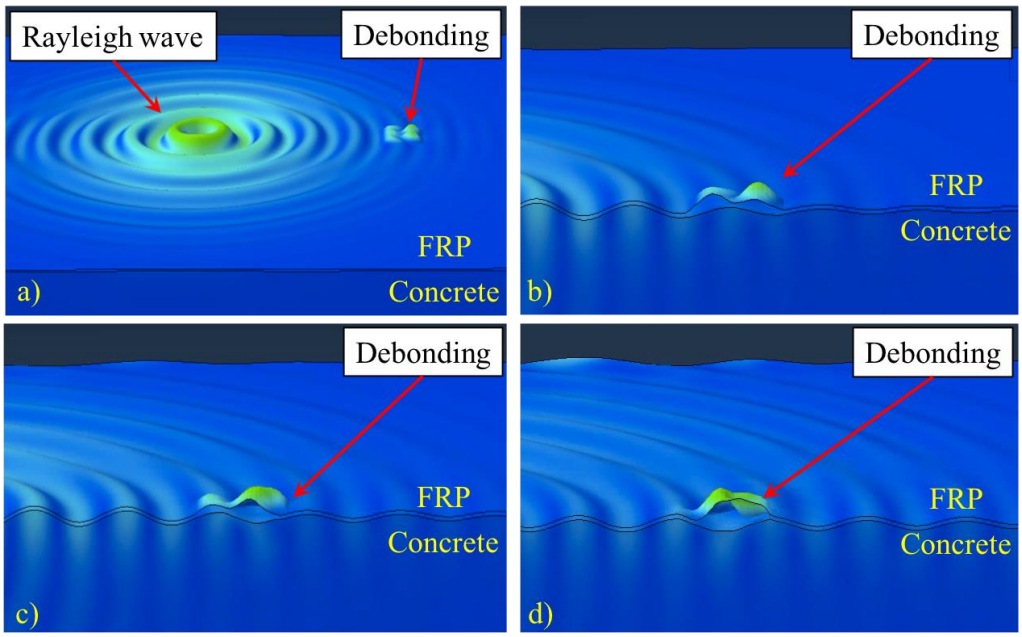

[**Figure 16**. Typical contour snapshots of FE simulated displacement at time a) t = 1.03×10^{-4}sec, b) the zoom-in of the cross-section at the debonding, c) t = 1.22×10^{-4}sec; and d) t = 1.41×10^{-4}sec]

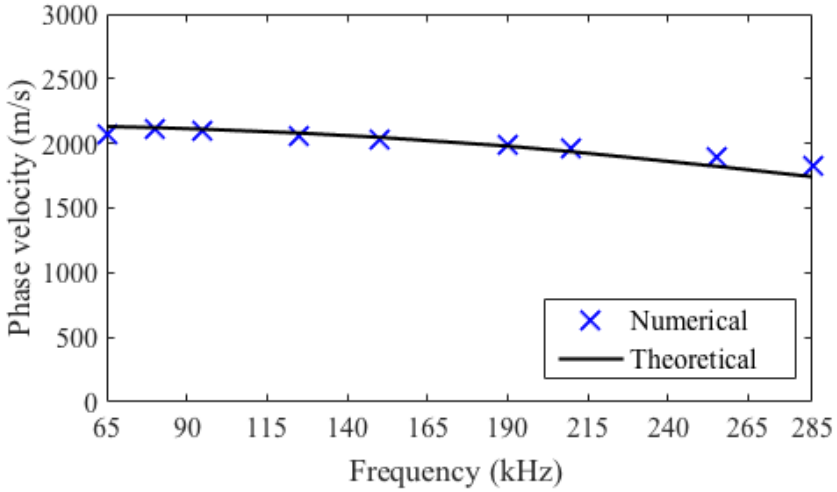

[**Figure 17**. Numerical and theoretical results of the Rayleigh wave phase velocity dispersion curve]

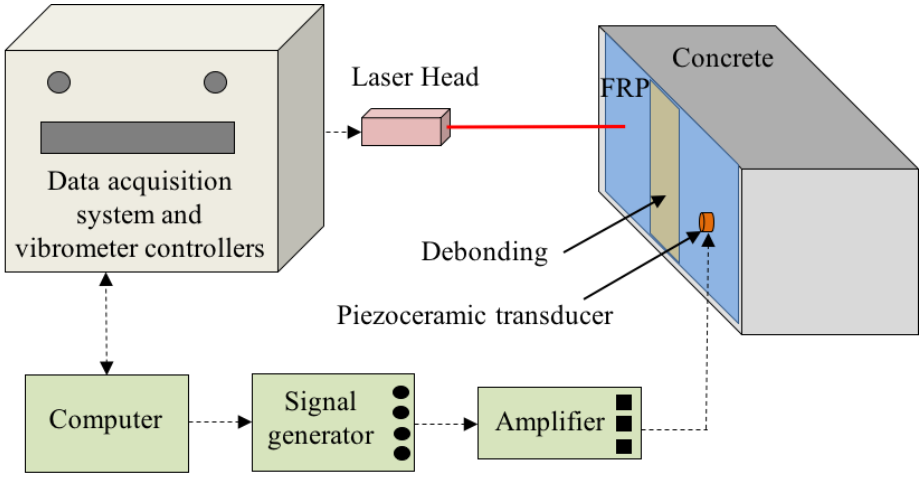

[**Figure 18**. Schematic diagram of experimental setup]

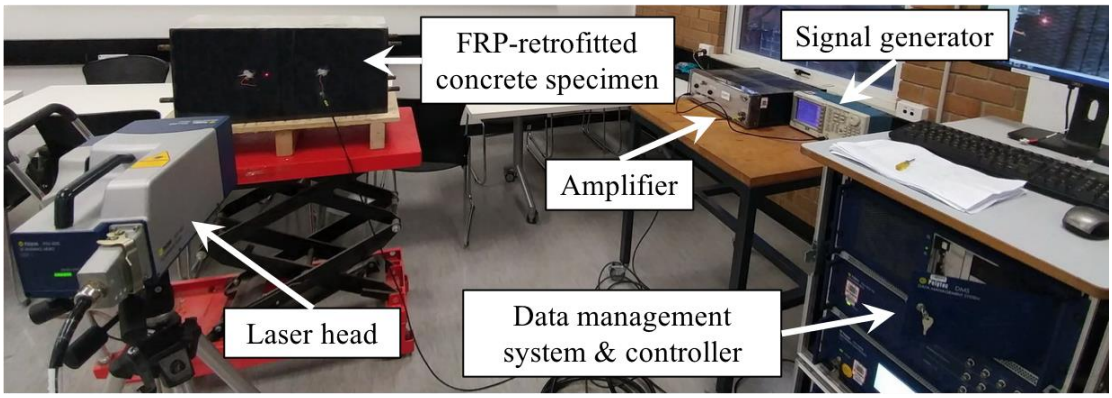

[**Figure 19**. Experimental setup and laser Doppler vibrometer]

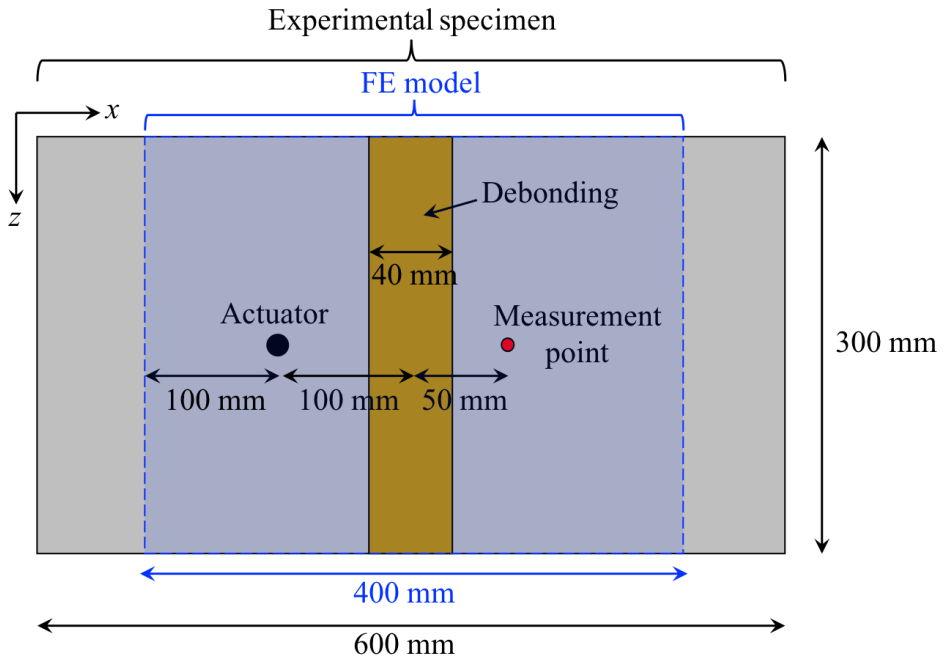

[**Figure 20**. FE model and experimental specimen used in the experimental validation]

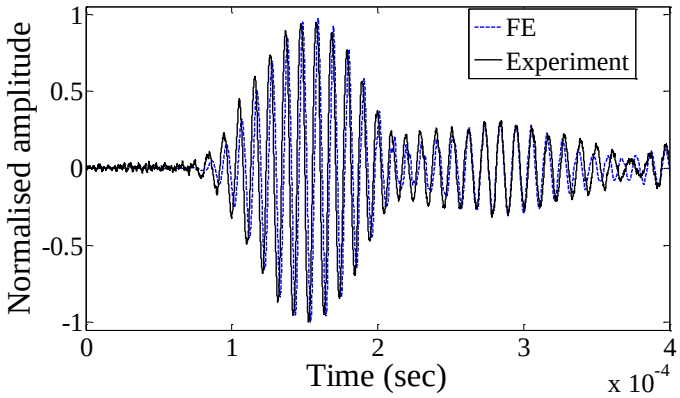

[**Figure 21**. Time-domain Rayleigh wave signal obtained from FE simulation and experimental measurement]

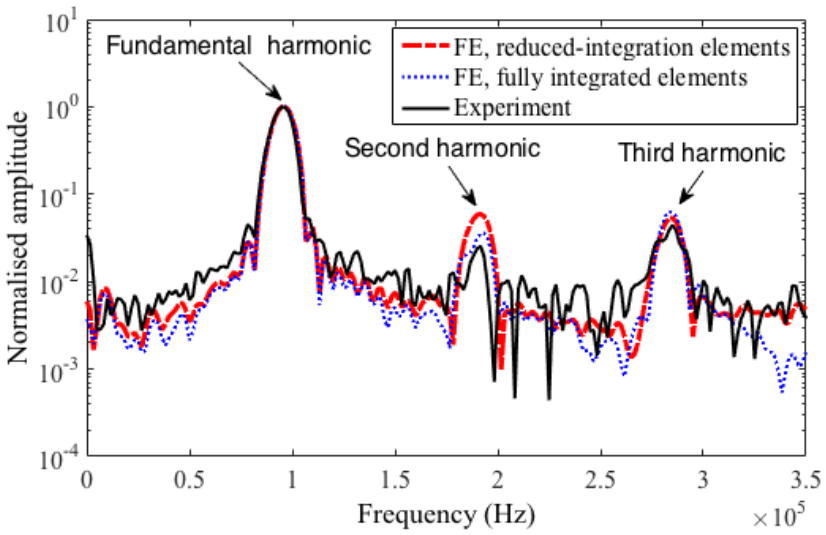

[**Figure 22**. Fourier transformed FE simulated and experimentally measured Ryleigh wave signals]

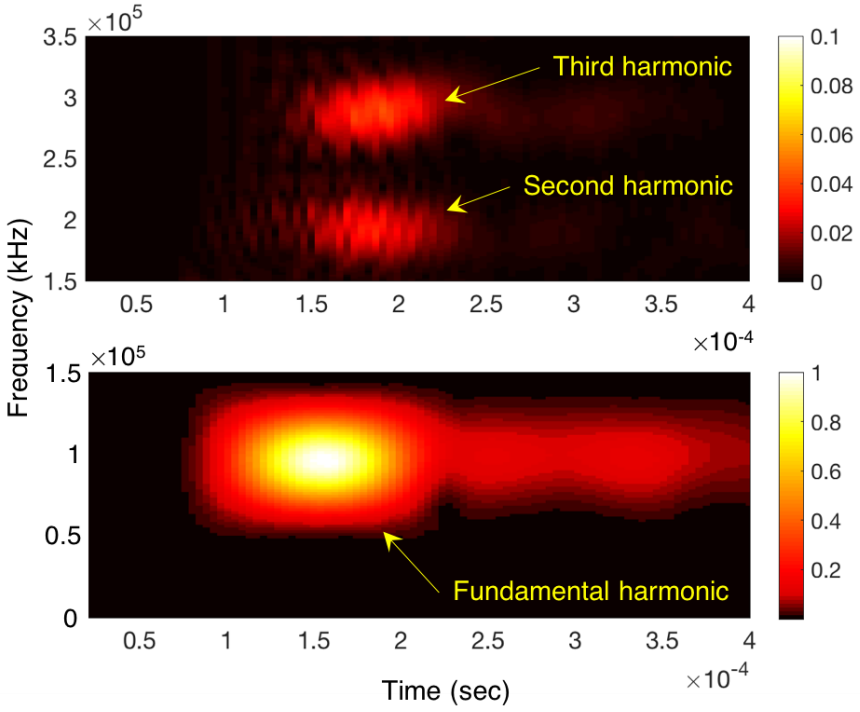

[**Figure 23**. Energy density spectrum in time-frequency domain for debonding size of 38mm×38 mm and θ =30°]

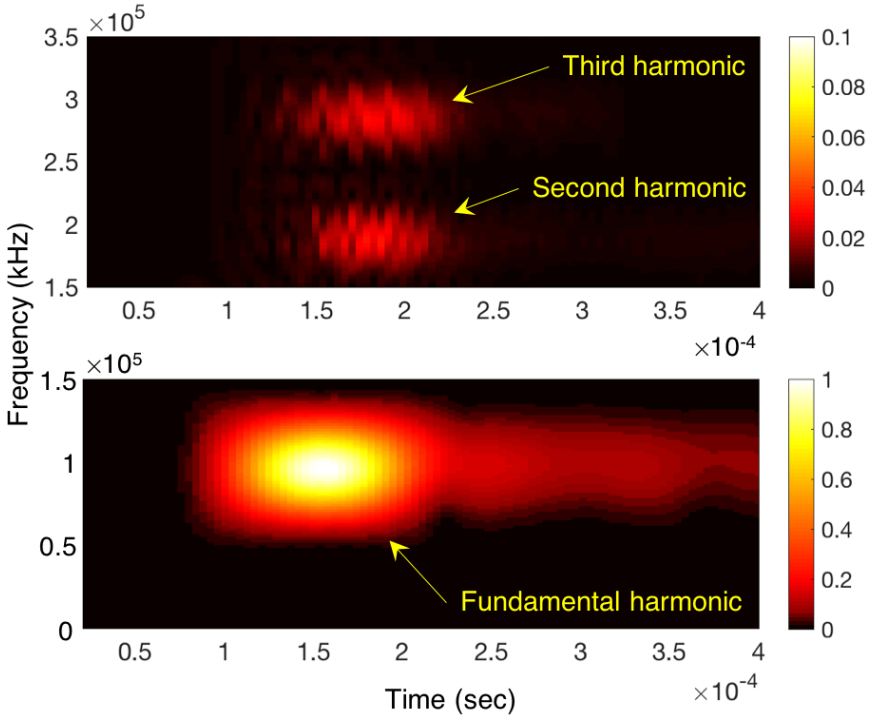

[**Figure 24**. Energy density spectrum in time-frequency domain for debonding size of 22mm×22 mm and θ =330°]

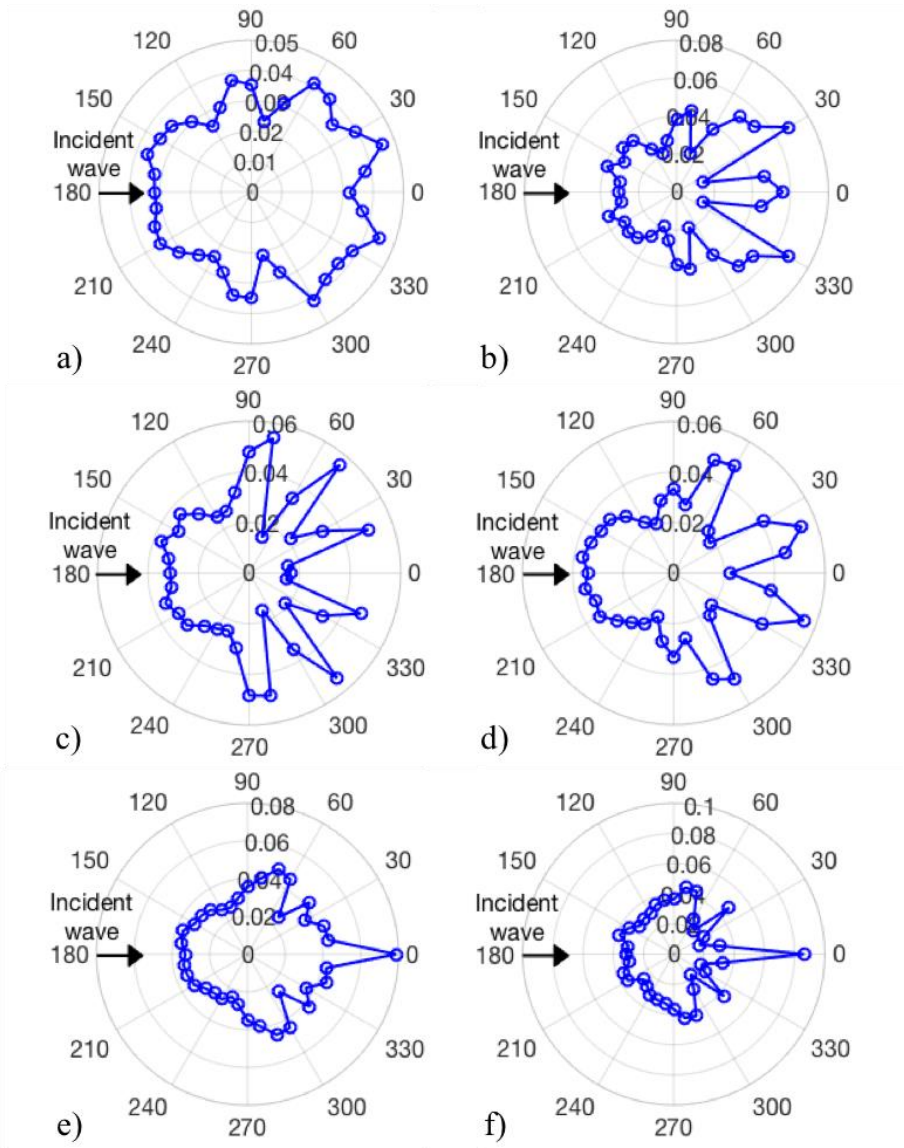

[**Figure 25**. Directivity pattern for second harmonic amplitude to fundamental harmonic amplitude ratio (A_2/A_1) for debonding size a) 8mm×8mm, b) 14mm×14mm, c) 22mm×22mm, d) 30mm×30mm, e) 38mm×38mm, and f) 44mm×44mm]

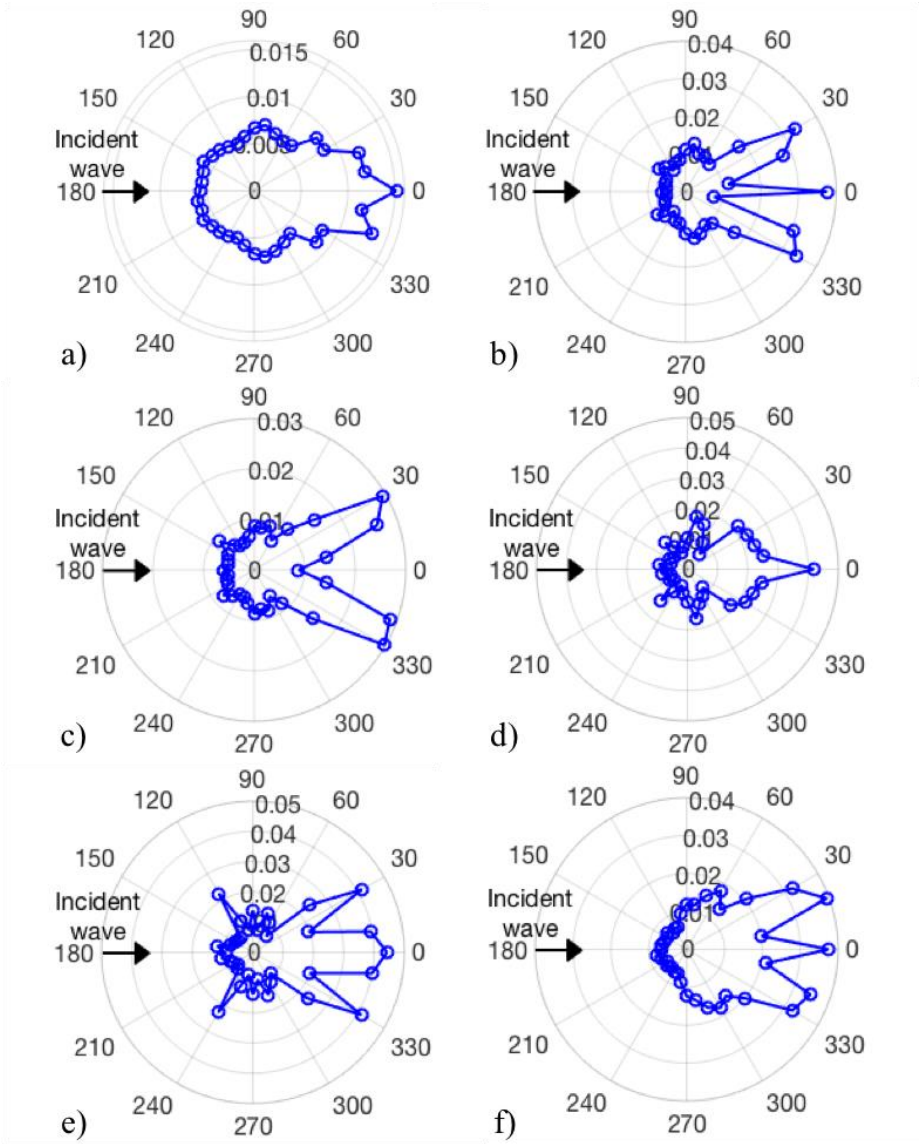

[**Figure 26**. Directivity pattern for third harmonic amplitude to fundamental harmonic amplitude ratio (A_3/A_1) for debonding size a) 8mm×8mm, b) 14mm×14mm, c) 22mm×22mm, d) 30mm×30mm, e) 38mm×38mm, and f) 44mm×44mm]

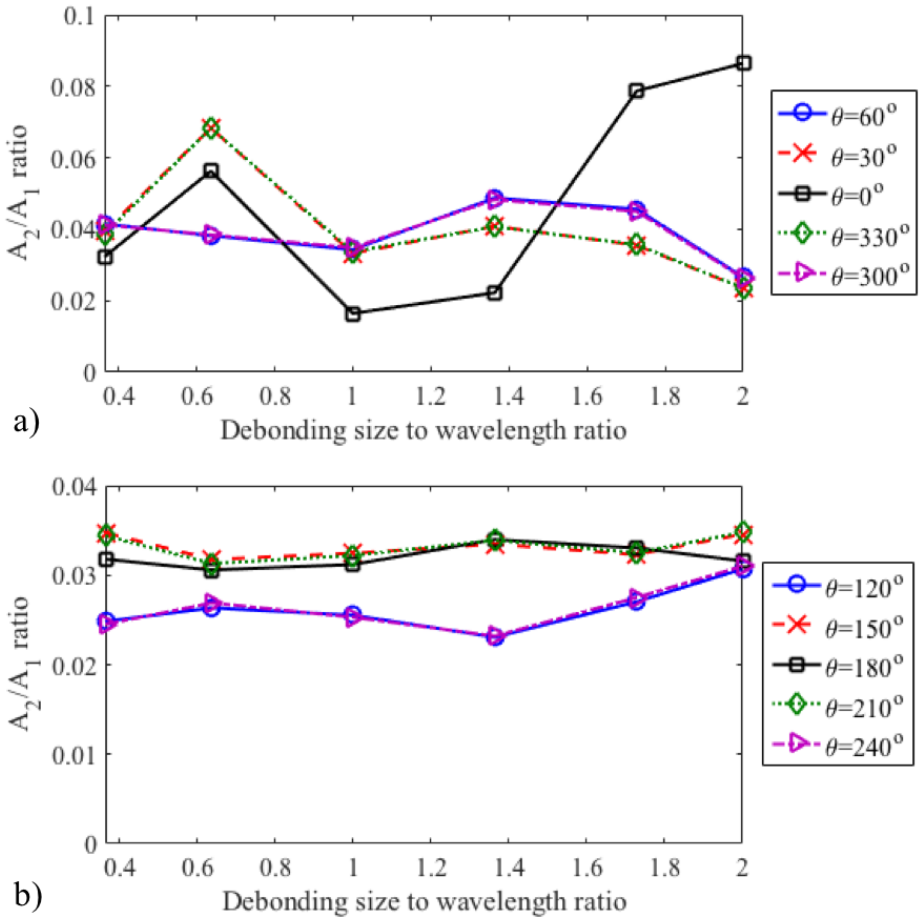

[**Figure 27**. Second harmonic amplitude to fundamental harmonic amplitude ratio (A_2/A_1) in the a) forward and b) backward scattering direction as a function of debonding size to wavelength ratio]

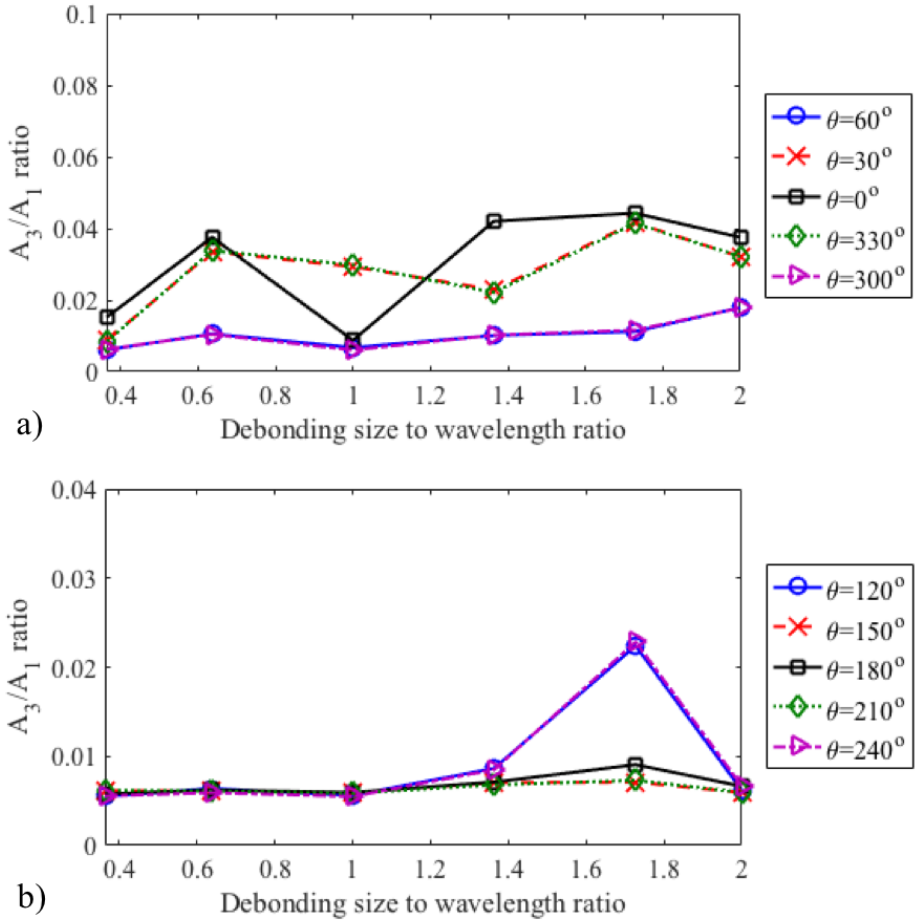

[**Figure 28**. Third harmonic amplitude to fundamental harmonic amplitude ratio (A_3/A_1) in the a) forward and b) backward scattering direction as a function of debonding size to wavelength ratio]